A Mechanism Leading to γ' Precipitates with 111 Facets and Unusual Orientation Relationships to the Matrix in γ–γ' Nickel-Based Superalloys

Suzanne Vernier, Jean-Michel Franchet, Christian Dumont, Nathalie Bozzolo

A mechanism leading to γ' precipitates with {111} facets and unusual orientation relationships to the matrix in γ/γ' nickel-based superalloys

Suzanne Vernier[a,b*], Jean-Michel Franchet[b], Christian Dumont[c] and Nathalie Bozzolo[a]

[a] MINES ParisTech, PSL – Research University, CEMEF – Centre de mise en forme des matériaux, CNRS UMR 7635, 1 rue Claude Daunesse, 06904 Sophia Antipolis, France
[b] Safran SA, Safran Tech – Materials & Process Department, Rue des Jeunes Bois – Châteaufort, 78772 Magny-les-Hameaux, France
[c] Aubert & Duval, Département R&D transformations, BP1, 63 770 Les Ancizes, France

*Corresponding author. suzanne.vernier@mines-paristech.fr

ABSTRACT

Cast-and-wrought heavily-alloyed γ-γ' nickel-based superalloys may exhibit large recovered grains inherited from the ingot conversion and characterized by a high density of close-to-coherent micrometric γ' precipitates. In the AD730™ nickel-based superalloy, a previous work [18] highlighted a new interaction between such precipitates and a recrystallization front passing through. This interaction resulted in γ' precipitates with a close-to-twin orientation relationship to their recrystallized host grain. Called T-type precipitates, they were revealed to be {111} bounded plate-like particles. The present paper aims to clarify the mechanism whereby such precipitates form. The formation of T-type precipitates actually is part of a more global mechanism which also produces γ' precipitates slightly misoriented from their surrounding matrix (C-type precipitates) and of same size and morphology as T-type precipitates. Both T and C type precipitates display {111} facets and are evidenced in the AD730™, René65 and PER72 alloys, supporting the idea that the mechanism can more generally occur in all low-lattice-mismatch γ-γ' nickel-based superalloys. Finally, a scenario is proposed: T/C type precipitates form at the recrystallization front of grains sharing a <111> axis with the recovered grain they consume, and develop {111} facets and specific orientations which minimize the interfacial energy on both recrystallized and recovered sides.

I. INTRODUCTION

Wrought polycrystalline γ-γ' nickel-based superalloys are commonly used to manufacture aero-engine turbine disks, thanks to their outstanding mechanical properties at high temperature [1,2]. Those alloys display γ grains and γ' precipitates of various sizes. The γ phase is a Face Centered Cubic (FCC) non-ordered solid solution, while the γ'-Ni_3(Al,Ti) phase has a $L1_2$ ordered cubic structure. At a few micrometers in size, primary precipitates are the largest precipitates of the microstructure [3]. Derived from the as-cast microstructure and high temperature billet forging sequences, they are useful for the grain size control since they pin grain boundaries during subsolvus forging operations. Most of the time, primary precipitates lie on grain boundaries and are incoherent with the surrounding γ matrix, which means that there is no matching at all between the γ' and the γ crystal lattices. Yet, the interaction between a recrystallization front and an incoherent precipitate is quite easy to predict. When a moving grain boundary encounters a precipitate, its curvature is locally modified due to capillarity effects, which is interpreted as a pinning force applied on the boundary and referred to as the Smith-Zener pinning force [4]. Then, if the grain boundary is subject to sufficient driving force to counteract the pinning force, it will bypass the precipitate; otherwise it will halt at the precipitate. However, when a moving boundary meets a coherent precipitate - which means that the γ and γ' crystal lattices perfectly coincide at the γ/γ' interface [5] - the interaction can be much more complex. Indeed, because coherent interfaces have low energy values [6,7], the maximum pinning force a coherent precipitate can enforce is twice that of an incoherent precipitate of the same size [8,9]. Then, other phenomena which also allow the grain boundary to carry on moving and which are more thermodynamically and/or kinetically interesting than the coherent precipitate bypass can occur. It was reported in the literature that a coherent precipitate may be cut-through - so that the orientation of the precipitate is changed to that of the growing grain [7,8] - or dissolved [10,11]. However, if the grain boundary driving force is not sufficient to bypass, dissolve or cut-through the coherent precipitate, the grain boundary will halt at the coherent precipitate which will then coarsen as a result of the interfacial energy equilibrium [8]. At a few hundred nanometers to few nanometers in size, secondary and tertiary precipitates are always coherent with their surrounding matrix. But much larger precipitates are also found coherent or close-to-coherent. First, Charpagne et al. evidenced large primary precipitates with the same orientation as their surrounding matrix in the case of heteroepitaxial recrystallization [12–14]. Second, cast-and-wrought heavily-alloyed γ-γ' nickel-based superalloys may exhibit unrecrystallized grains inherited from the ingot conversion process[15–17] where a high density of micrometric close-to-coherent precipitates is found. These unrecystallized grains are characterized by intragranular orientation gradients with more or less developed recovery cell structures; thus they will be called recovered grains in the following text. Yet, in the AD730™ γ-γ' nickel-based superalloy a previous work [18] pointed out a new interaction between the close-to-coherent precipitates of the recovered grain and the recrystallization front passing through. This interaction sometimes led to γ' precipitates with a close-to-twin orientation relationship to their recrystallized host grain. "Close to twin orientation relationship" means that the γ' and γ cubic lattice cells conform to a 60°<111> rotation within the 8.66° tolerance given by Brandon's criterion: both the misorientation angle and misorientation axis do not deviate more than 8.66° to the 60° angle and <111> axis of the perfect twin boundary [18,19]. Such precipitates close to the twin orientation relationship have been called T-type precipitates and revealed to be {111} bounded plate-like particles. Their size, morphology and narrow orientation spread compared to the precipitates of the recovered grain have proved that they do not result from a simple bypass by the recrystallization front but from a specific mechanism. The aim of

the present paper is to clarify this mechanism using EBSD data analyses. It is shown that the formation of T-type precipitates is part of a more global mechanism which also produces precipitates with an orientation very close to that of their surrounding matrix and of the same size and morphology as the T-type precipitates. These precipitates are called C-type precipitates and rotated by few degrees around a <111> axis they have in common with their surrounding matrix. T and C type precipitates are evidenced in the AD730™, René65 and PER72 alloys, supporting the idea that the studied mechanism can more generally occur in all γ-γ' nickel-based superalloys with a low-lattice mismatch. Finally, a scenario is proposed for this specific mechanism which allows a recrystallization front to get through a high density of close-to-coherent micrometric precipitates and leads to γ' precipitates with unusual morphologies and orientations.

II. EXPERIMENTAL

In the present paper, five samples are analyzed. They are derived from different thermo-mechanical conditions and from three different alloys: AD730™, René65 and PER72. The PER72 alloy is an equivalent of the Udimet720 alloy manufactured by the Aubert&Duval Company. All these polycrystalline γ-γ' nickel-based alloys are all heavily-alloyed, derived from the traditional cast-and-wrought route and characterized by a low lattice mismatch [12,20] . Their chemical compositions are given in Table 1.

Three samples were cut out from AD730™ billets. Two of them were observed as-received. The third one, referred to as the "AD730™ Lab-Forged sample", was deformed at high temperature (compression test) then solution-treated for 4 hours at 1080°C in order to complete recrystallization. Hot-deformation and solution-treatment temperatures were both below the γ' solvus temperature which is about 1110°C. The fourth and fifth samples were cut out from René65 and PER72 billets and heat-treated for two hours at about 40° below their respective γ' solvus temperature. All the samples were ground with Si papers and polished with diamond suspensions down to 1µm. To obtain a suitable surface quality for EBSD (Electron BackScatter Diffraction), they were finally polished either by electropolishing (electrolyte: CH_3OH-10% $HClO_4$) or with a 0.02µm colloidal silica solution on a vibratory machine. Observations were carried out with a Zeiss Supra40 Field Emission Gun Scanning Electron Microscope operated at 15kV. The microscope is equipped with the QUANTAX EDS/EBSD system from the Bruker Company which is composed of an XFlash 5030 Energy Dispersive X-ray Spectrometer (EDS) and an e$^-$FlashHR EBSD detector, both controlled by the ESPRIT® software package. Some of the EBSD data post-treatments were performed using MTEX, a freely available MATLAB toolbox [21].

III. RESULTS AND DISCUSSION

A. T and C type precipitates in the AD730™ alloy : the results of a single mechanism

T-type precipitates have been reported in the alloy AD730™, in some recrystallized grains which had extensively grown into a recovered grain and which shared a <111>axis with it [18]. Nevertheless, Fig.1 shows that T-type precipitates are not the only type of precipitate which can be found in such recrystallized grains. Indeed, some precipitates which are 2-3° misoriented from their host grain appear among the T-type precipitates (Fig.1.a). These precipitates have a nearly rectangular shape in the sample section like the T-type precipitates (Fig.1.b). Close to the orientation of their surrounding matrix, they will be called C-type precipitates in the

following text. The rectangular shapes of the C-type precipitates are parallel and also parallel to those of the T-type precipitates (Fig.1.b). On the {111} pole figure (Fig.1.d), the orientations of T and C type precipitates (randomly selected) are compared to those of the host recrystallized grain and the recovered grain. First, the orientations of the two precipitate types appear very homogeneous compared to those of the recovered grain selected over a much smaller area. Second, the <111> axis shared by the recrystallized and recovered grains perfectly matches with a <111> axis of the C and T type precipitates. Indeed, the three other <111> axes of the C type precipitates differ slightly from those of their recrystallized host grain, showing that the misorientation of the C-type precipitates regarding their host grain originates from a rotation of few degrees around the <111> axis they exactly have in common. Moreover, the longest sides of the rectangular shapes of the T and C type precipitates are parallel to the {111} plane trace common to the recrystallized and recovered grains. Yet, it has been evidenced in [18] that T-type precipitates are plate-like particles bounded by the {111} plane common to the T-type precipitates, the recrystallized grain and the recovered grain. Here, the similar morphologies and alignments of the C and T type precipitates strongly suggests that both types of precipitates are facetted by the same {111} plane, common to the recrystallized and recovered grains.

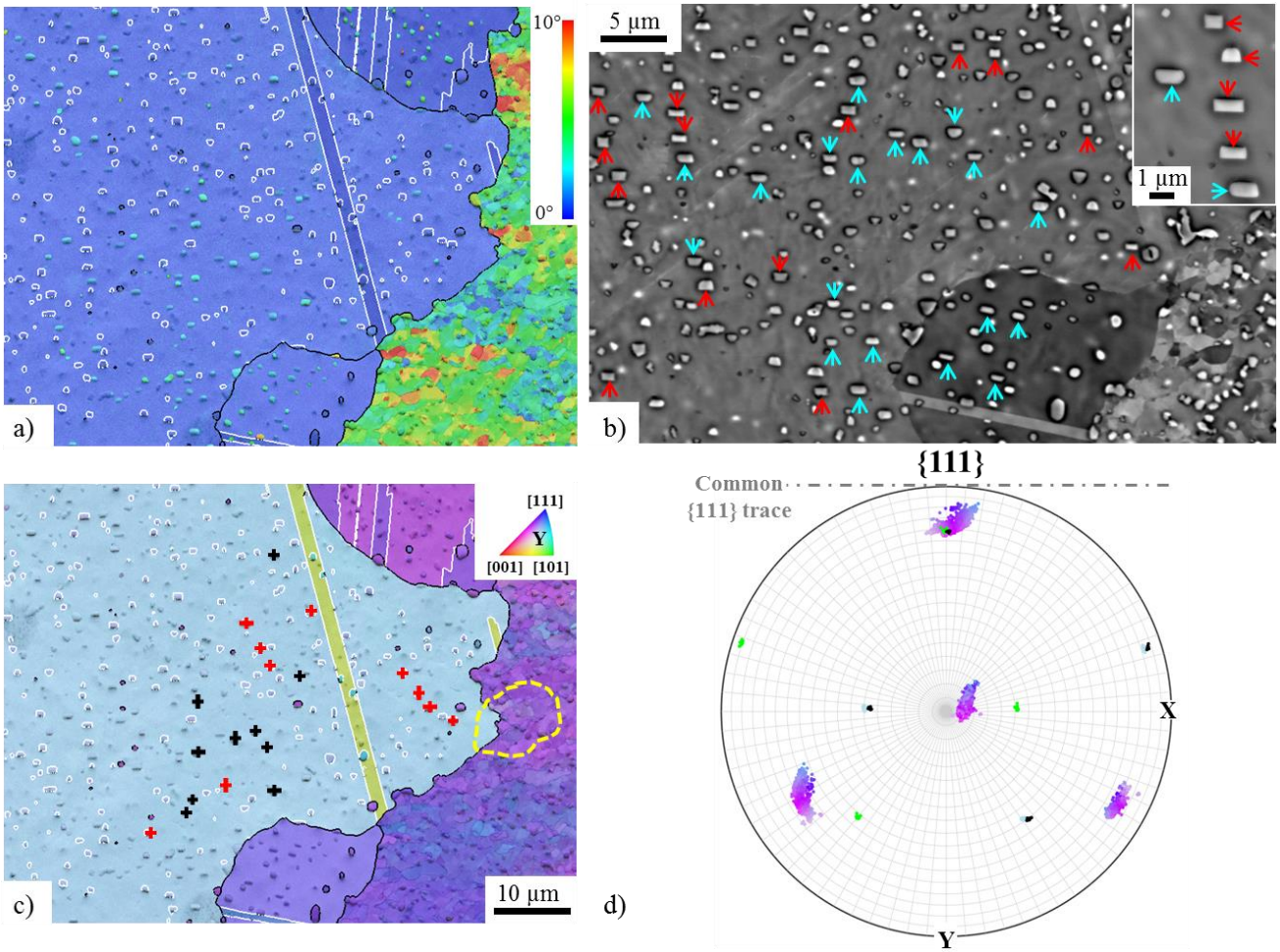

Fig.1 – C and T type precipitates coexisting in a recrystallized grain (AD730™ Lab-Forged sample). a) EBSD map: misorientation angle to the mean orientation of the grain overlaid on the band contrast map, grain boundaries (misorientation angle threshold: 10°) plotted black and twin boundaries (60°<111> with 8.66° tolerance, following Brandon's criterion [19]) plotted white. b) Backscattered electron image, where the γ' precipitates appear bright despite their lower atomic number because of topographic effects induced by electropolishing. Some C and T type precipitates are highlighted by blue and red arrows respectively. c) EBSD

map: orientation (IPF color code) overlaid on the band contrast map, grain boundaries plotted black and twin boundaries plotted white. d) {111} pole figure on a spherical grid (spacing: 5°), orientations of ten C-type precipitates (black crosses in c)) plotted black, orientations of ten T-type precipitates (red crosses in c)) plotted green and orientations of the yellow selection in c) plotted with the same color as displayed in c). The {111} *plane trace common to the C/T type precipitates and the recrystallized matrix is displayed by a dashed line.*

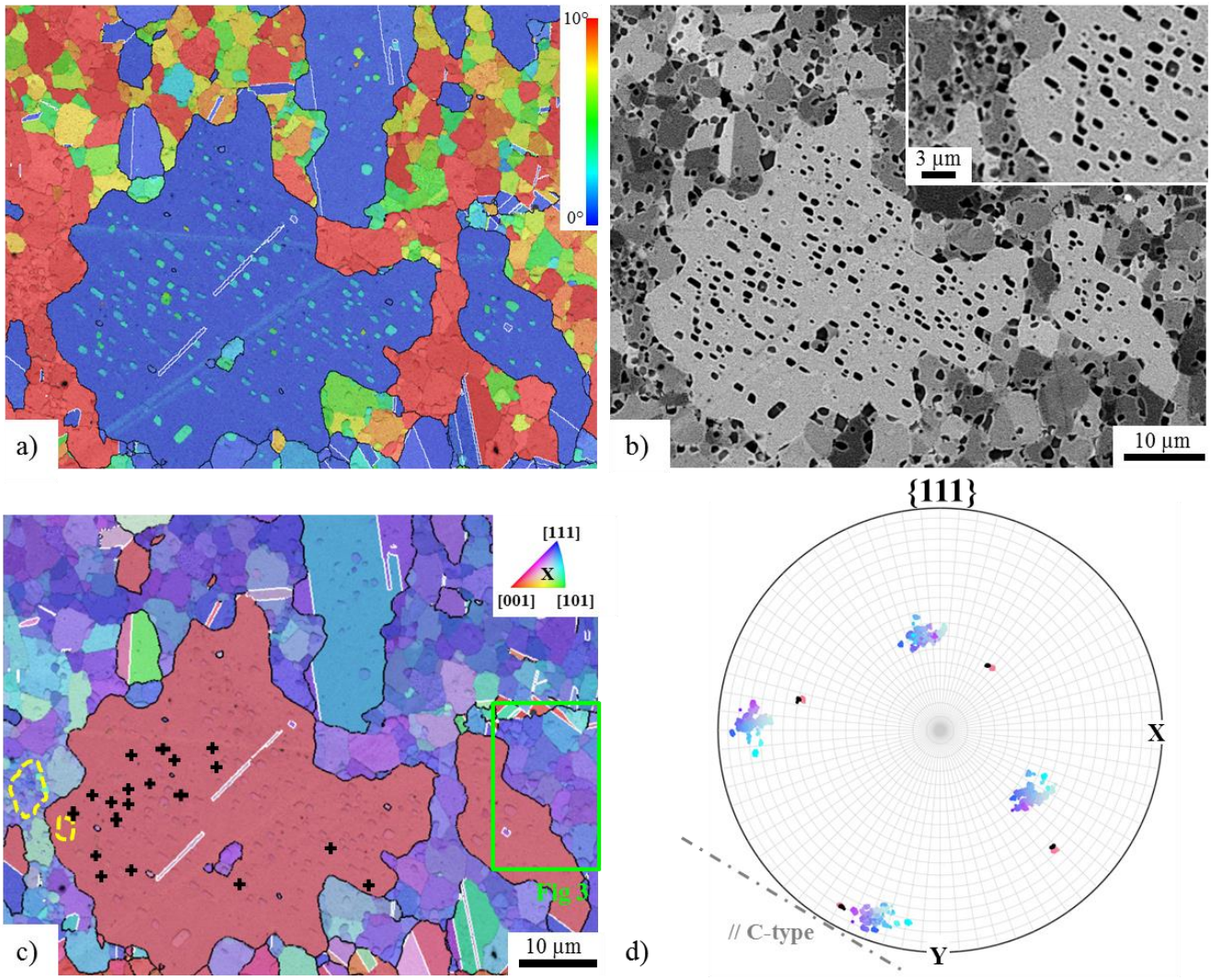

Fig.2 – Grain full of C-type precipitates (AD730™ billet sample). a) EBSD map: misorientation angle to the mean orientation of the grain overlaid on the band contrast map, grain boundaries (misorientation angle threshold: 10°) plotted black and twin boundaries (60°<111> with 8.66° tolerance) plotted white. b) Backscattered electron image. c) EBSD map: orientation (IPF color code) overlaid on the band contrast map, grain boundaries plotted black and twin boundaries plotted white. d) {111} pole figure on a spherical grid (spacing: 5°), orientation of the selected C type precipitates (black crosses in c)) plotted black, orientations of the yellow selections in c) plotted with the same color as displayed in c). The {111} plane trace common to the C type precipitates and the recrystallized matrix is displayed by a dashed line.

Fig. 2 presents an example of a large recrystallized grain with a single T-type precipitate amongst many C-type precipitates in an AD730™ billet. The recrystallized grain has grown by consuming a so-called substructured grain, which is a former grain mainly composed of well-defined low-misoriented crystallites with micrometric close-to-coherent precipitates located at their boundaries. It is worth mentioning here that the close-to-coherent precipitates of the substructured grain are not C-type precipitates since they do not have the aligned rectangular shapes and narrow orientation spread of the neighboring C-type precipitates (Fig.2.b and Fig.3). The

substructured and recrystallized grains have a <111> axis close to each other (Fig.2.d), so that the recrystallized grain is rotated around this <111> axis with respect to the substructured grain, but less rotated than what has been observed in Fig.1. This <111> axis also coincides with the <111> axis around which the orientations of the C-type precipitates are rotated relatively to that of their host grain. Moreover, the corresponding {111} plane trace is parallel to the longest sides of the C-type precipitates, which is again consistent with C-type precipitates bounded by {111} planes.

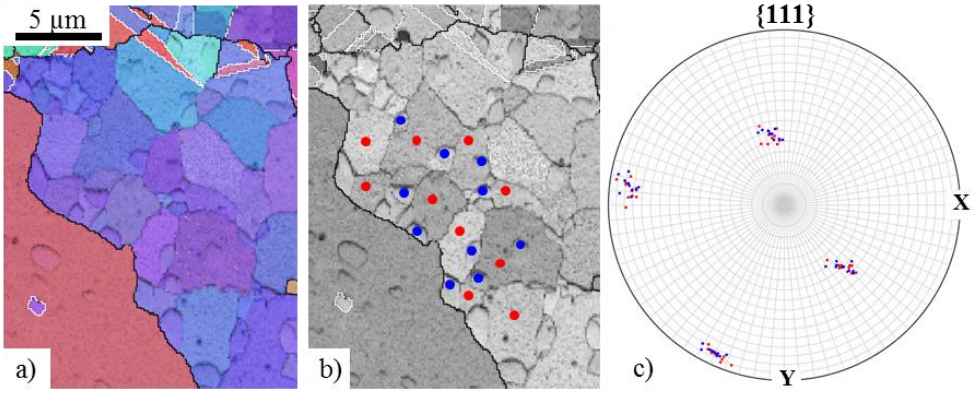

Fig.3 – Orientations of the precipitates in the substructured grain with respect to their surrounding matrix (AD730™ billet sample – Area highlighted in Fig.2.c). a) EBSD map: orientation (IPF color code) overlaid on the band contrast map, grain boundaries (misorientation angle threshold: 10°) plotted black and twin boundaries (60°<111> with 8.66° tolerance) plotted white. b) EBSD map: band contrast map, grain boundaries plotted black and twin boundaries plotted white. c) {111} pole figure on a spherical grid (spacing: 5°). Orientation of the precipitates (selected by blue points in b)) plotted blue, orientations of the matrix (selected by red points in b)) plotted red.

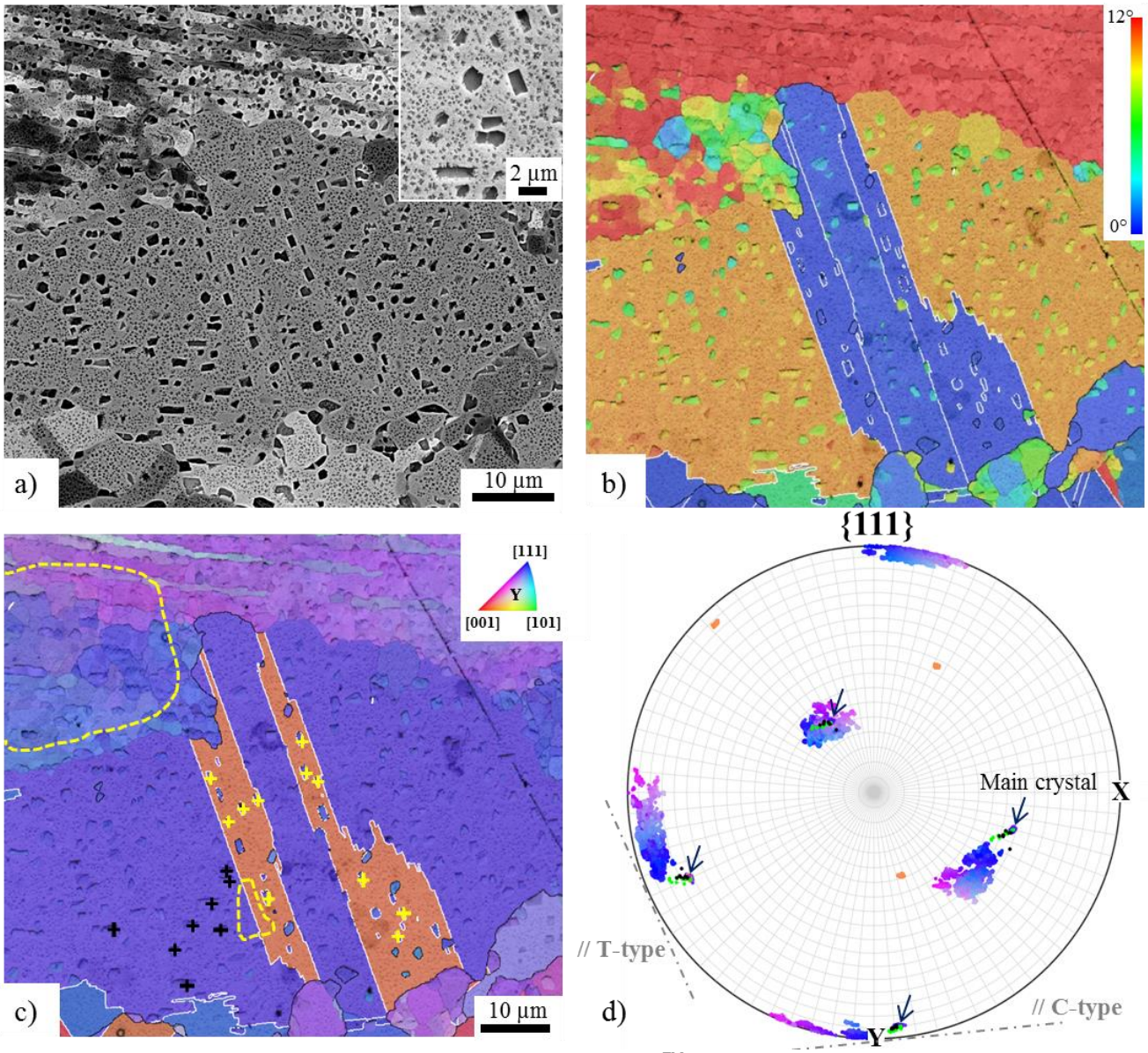

Fig.4 – Change from C type to T type precipitates by twinning (AD730™ billet sample). a) Backscattered electron image (overall view) and secondary electron image (insert at high magnification). b) EBSD map: misorientation angle to the mean orientation of the grain overlaid on the band contrast map, grain boundaries (misorientation angle threshold: 10°) plotted black and twin boundaries (60°<111> with 8.66° tolerance) plotted white. c) EBSD map: orientation (IPF color code) overlaid on the band contrast map, grain boundaries plotted black and twin boundaries plotted white. d) {111} pole figure on a spherical grid (spacing: 5°), orientations of the C-type precipitates (black crosses in c)) plotted black, orientations of the T-type precipitates (yellow crosses in c)) plotted green and orientations of the yellow selections in c) plotted with the same color as displayed in c). The {111} plane traces common to the C/T type precipitates and the recrystallized matrix are displayed by dashed lines.

A last example of C and T type precipitate coexistence in the AD730™ alloy is presented in Fig.4. This time, a large recrystallized grain consuming a recovered grain displays C-type precipitates in its main crystal and T-type precipitates in its twin crystals (Fig.4.b). The two precipitate types are again rectangular in the sample section and can reach few micrometers in length. However, the rectangular shapes of the T and C type precipitates follow two different directions in space. The {111} pole figure (Fig.4.d) reveals that the main crystal has an orientation very close to that of the recovered grain and that the longest sides of the C-type precipitates are not so

far from a {111} plane trace. The twin crystals have a single <111> axis in common with the recovered grain and the longest sides of the T-type precipitates coincide with the corresponding {111} plane trace (which differs from that of the C-type precipitate). In this third example, the orientations of the C-type precipitates are very homogeneous but those of the selected T-type precipitates are somewhat more spread than observed in Fig.1. This underlines that the mechanism leading to T-type precipitates does not produce perfect twin boundaries.
For the three cases presented above, as well as for the cases which will be presented in the following sections, the misorientation between the recrystallized grain and the recovered (or substructured) grain has been quantified by calculating the average misorientation angle ($\bar{\theta}$) at the recrystallized/recovered boundary (average on boundary segments of at least few tens of micrometers long). The values are summarized in Table 2. From Table 2, it can be noticed that recrystallized grains whose misorientation to the recovered grain is lower than ~37° show C-type precipitates only. On the other hand, recrystallized grains which are misoriented by more than ~50° show T-type precipitates only. Between these two misorientation angles, a transition zone is observed where recrystallized grains exhibit both C and T type precipitates. So, although a more statistical analysis would be required to obtain more precise transition values, there does exist a link between the misorientation angle of the recrystallized grain relatively to the recovered grain and the precipitate type(s) which form(s).

To summarize, the C and T type precipitates are located in recrystallized grains which have grown into recovered/substructured grains. Both can display rectangular shapes in sample sections. If so, the longest sides of their rectangular shapes are up to a few micrometers in length and parallel to the trace of the {111} plane they share with their host grain. The corresponding shared <111> axis is always very close to a <111> axis of the consumed recovered/substructured grain. Thus, C and T type precipitates are both {111} bounded plate-like particles which derive from the same mechanism. The misorientation angle between the recrystallized and the recovered grains determines what precipitate type forms: while the less misoriented recrystallized grains only display C-type precipitates, the highest misoriented recrystallized grains display only T-type precipitates, and intermediate misorientations both types. Recrystallized grains with a <111> axis very close to one of the <111> axes of the recovered grain they consume originate from the Continuous Recrystallization (CRX) and the Heteroepitaxial Recrystallization (HERX) which are the two recrystallization mechanisms identified for the recovered grains of the AD730^{TM} alloy [18]. Both mechanisms produce recrystallized grains whose initial orientations are close to that of the recovered grain. As the recrystallized grain grows into the recovered grain, its misorientation with respect to the recovered grain increases because of the orientation gradients present inside the recovered grain. By growing, the recrystallized grain may also undergo annealing twinning, so that the misorientation of the recrystallization front changes from a rather low misorientation to a high one (or conversely) due to the additional 60° <111> rotation. This explains why a wide range of misorientation angles is observed at the recrystallized/recovered boundaries (Table 2).

B. Observations in other γ/γ' superalloys: René65 and PER72 alloys

In René65 and PER72 billets, recovered grains with their characteristic high density of close-to-coherent precipitates can also be observed (Fig.5.a and Fig.7.a). Besides, the configuration presented in Fig.1for the AD730^{TM} alloy is found in the René65 billet sample too (Fig.5): a few large recrystallized grains have grown to a large extent inside a recovered grain. These large recrystallized grains are full of micrometric precipitates with

some of them well rectangular in the sample section (Fig.5.d-e). Some of the rectangular precipitates are in twin orientation relationship to their host grain but the twin orientation relationship is imperfect because only realized within the 8.66° tolerance given by Brandon's criterion (Fig.6). Thus, such precipitates do correspond to the T-type precipitates as defined in the alloy AD730™. In the same crystal, rectangular precipitates slightly-misoriented to their surrounding matrix and parallel to the T-type precipitates are also found (Fig.5.d-e): these precipitates are C-type precipitates. On the {111} pole figure (Fig.5.c), one can check that the crystal hosting the T and C type precipitates has a <111> axis very close to a <111> axis of the recovered grain. Then, T and C type precipitates are rotated around this common <111> axis with respect to their host grain and the corresponding {111} plane trace coincides with the longest sides of their rectangular shapes. As observed in the AD730™ alloy, the orientations of the two precipitate types are more homogeneous than that of the recovered grain. Finally, CRX cells and HERX grains can be noticed at the borders of the recovered grain (black and white arrows in Fig.5.a).

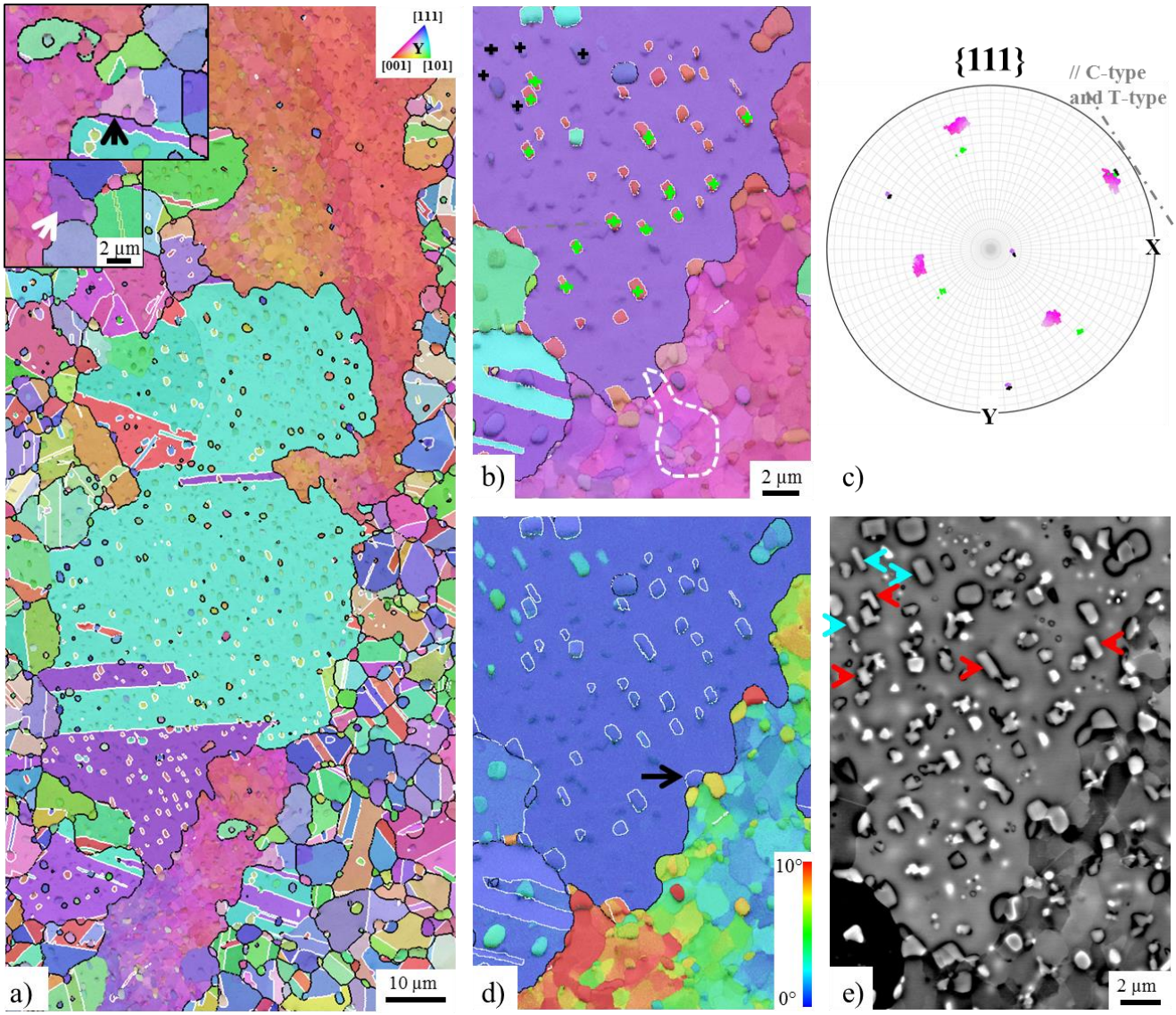

Fig.5 – C and T type precipitates resulting from the recrystallization of a recovered grain in the René65 alloy (René65 billet sample). a) and b) EBSD map: orientation (IPF color code) overlaid on the band contrast map, grain boundaries (misorientation angle threshold: 10°) plotted black and twin boundaries (60°<111> with 8.66° tolerance) plotted white. In the inserts, the black and white arrows underline a CRX cell and a HERX grain

respectively. c) {111} pole figure on a spherical grid (spacing: 5°), orientations of the C-type precipitates (black crosses in b)) plotted black, orientations of the T-type precipitates (green crosses in b)) plotted green and orientations of the white selection in b) plotted with the same color as displayed in b). The {111} plane trace common to the C/T type precipitates and the recrystallized matrix is displayed by a dashed line. d) EBSD map: misorientation angle to the mean orientation of the grain overlaid on the band contrast map, grain boundaries plotted black and twin boundaries plotted white. The black arrow underlines a T-type precipitate at the recrystallization front. e) Backscattered electron image, where the γ' precipitates appear bright despite their lower atomic number because of topographic effects induced by electropolishing. C and T type precipitates are highlighted by blue and red arrows respectively.

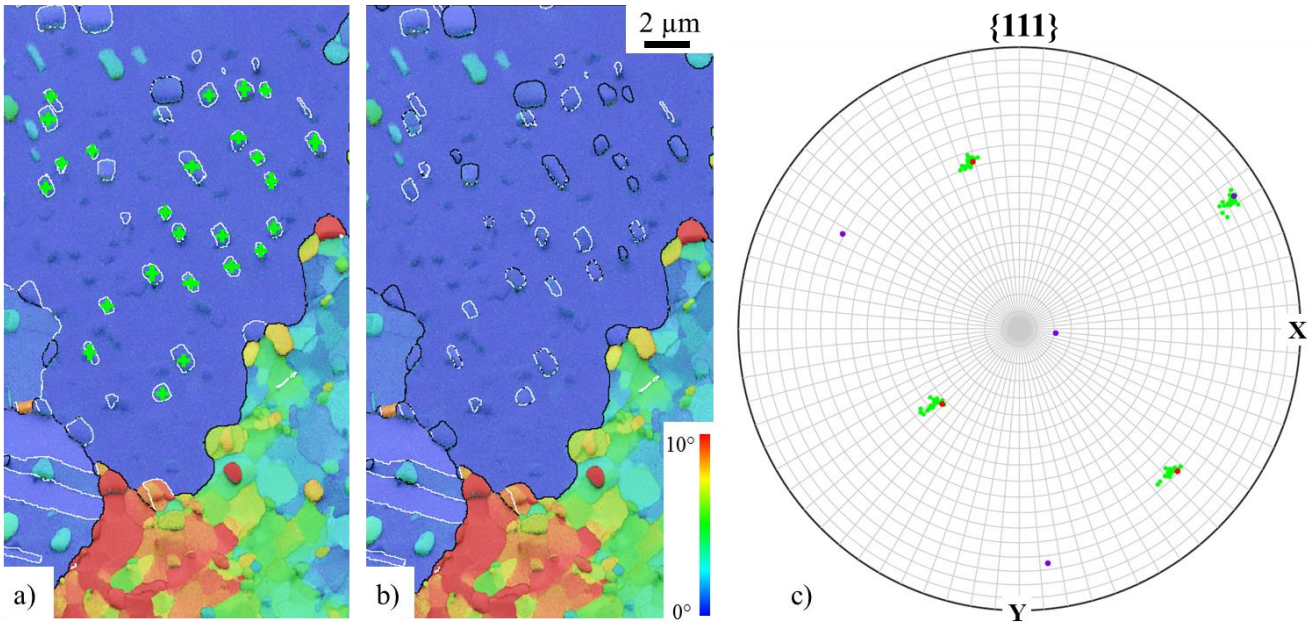

Fig.6 – The imperfect twin orientation relationship of the T-type precipitates (René65 billet sample). a) and b) EBSD maps - misorientation angle to the mean orientation of the grain overlaid on the band contrast map, grain boundaries (misorientation angle threshold: 10°) plotted black and twin boundaries (60°<111> with Δθ tolerance) plotted white. In a) twin boundaries are plotted with 8.66° tolerance following Brandon's criterion [19]. In b) twin boundaries are plotted with 2° tolerance. c) {111} pole figure on a spherical grid (spacing: 5°). The orientations of the T-type precipitates selected in a) are plotted green, the orientations of the surrounding matrix and the corresponding perfect twin crystal (60°<111> 0° tolerance) are plotted purple and red respectively.

No case of striking heterogeneous recrystallization with large recrystallized grains full of T/C type precipitates has been observed in the studied PER72 billet sample. It is also worth mentioning here that, in the AD730™ and René65 alloys, all the recovered grains do not always lead to several huge statically recrystallized grains as shown throughout the paper. The reason why this phenomenon is not systematic is not understood yet but would be interesting to investigate in future research. Nevertheless, in the PER72 alloy, isolated T and C type precipitates are seen in recrystallized grains of "normal" size next to recovered grains (red and blue arrows in Fig.7). For example, the yellow grain on Fig.7.a contains several C and T type precipitates. This grain has a <111> axis not so far from a <111> axis of the nearby recovered grain (dashed circle in Fig.7.b), although it is not the twin axis of the T-type precipitates. Some CRX cells and HERX grains are also seen in the recovered grains of the PER72 alloy (white and yellow arrows in Fig.7). This means that the two recrystallization mechanisms suspected in the AD730™ alloy as taking part to the formation of the T/C type precipitates also occur in the PER72 alloy.

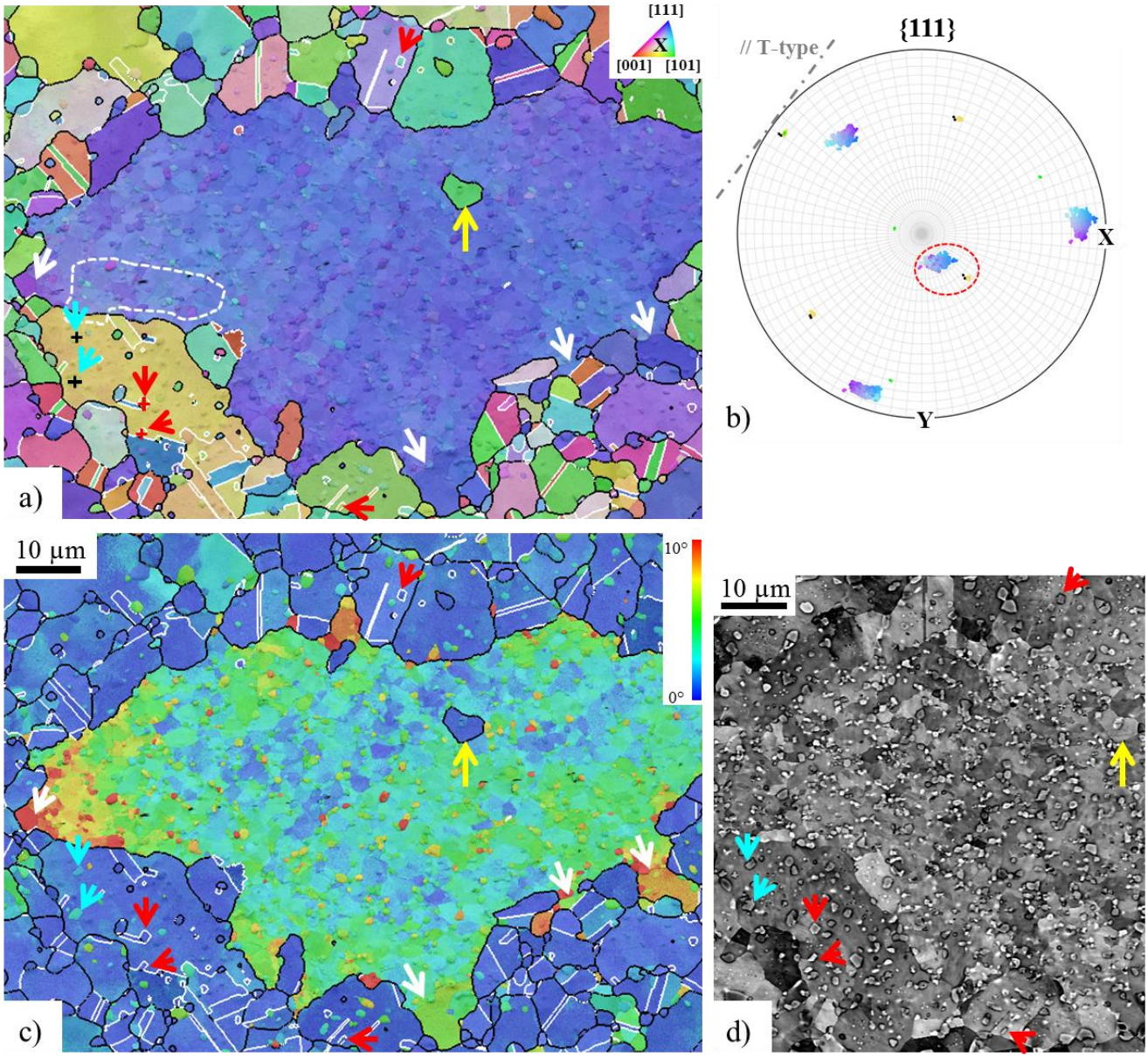

Fig.7 – A recovered grain in the PER72 *alloy (*PER72 *billet sample). a) EBSD map: orientation (IPF color code) overlaid on the band contrast map, grain boundaries (misorientation angle threshold: 10°) plotted black and twin boundaries (60°<111> with 8.66° tolerance) plotted white. b) {111} pole figure on a spherical grid (spacing: 5°), orientations of the C-type precipitates (black crosses in a)) plotted black, orientations of the T-type precipitates (red crosses in a)) plotted green and orientations of the white selection in a) plotted with the same color as displayed in a). A {111} plane trace is displayed by a dashed line. c) EBSD map: misorientation angle to the mean orientation of the grain overlaid on the band contrast map, grain boundaries plotted black and twin boundaries plotted white. d) Backscattered electron image, where the γ' precipitates appear bright despite their lower atomic number because of topographic effects induced by electropolishing. Red, blue, yellow and white arrows highlight T-type precipitates, C-type precipitates, HERX grain and CRX cells respectively.*

Thus, T and C type precipitates, with their characteristic {111} facets and orientation relationships, can be identified in recrystallized grains near the recovered grains of the René65 and PER72 alloys. In the same way as in the AD730^{TM} alloy, the recrystallized host grain has a <111> axis very close to a <111> axis of the nearby recovered grain. Such recrystallized grains are very likely to derive from the CRX and HERX which occur in the recovered grains of the three alloys studied.

C. Clarification of the mechanism leading to T and C type precipitates

1. An advantageous mechanism to overcome a high density of close-to-coherent precipitates

Fig.8 displays several large recrystallized grains which have extensively grown by consuming the nearby recovered grain. If the crystallographic orientations of these recrystallized grains (labelled by black stars in Fig.8.a) are compared to those of the recovered grain (Fig.8.c), it appears that all the recrystallized grains – except the grain N°1 in Fig.8.a – have a <111> axis close to a <111> axis of the recovered grain they consume (less than 10° deviation). Moreover, all these large recrystallized grains show a high density of intragranular precipitates which are C and/or T type precipitates (Fig.8.b).

On the other hand, many recrystallized grains attempting to consume a recovered grain remain very small (Fig. 9). If some of the small recrystallized grains can result from the CRX and HERX occurring in recovered grains, many of them derive from Discontinuous Recrystallization (DRX) [22] and so have random orientations, especially those at the periphery of the recovered grain. Nevertheless, whatever the origin of the small recrystallized grains, each time the same pattern is noticed: i) recrystallized grains are small but larger than the recovery cells of the recovered grain (which are delimited by close-to-coherent precipitates); ii) small recrystallized grains are free from precipitates (except the precipitate which originated HERX); iii) some coarse close-to-coherent precipitates can be pointed out on the boundaries of the small recrystallized grains. From this pattern, a scenario explaining why these recrystallized grains remain so small may be developed. Given that small recrystallized grains are always larger than recovery cells, they must start growing by dissolving the nearby close-to-coherent precipitates. But, since no re-precipitation is observed behind the recrystallization front, at first time all the γ'-forming elements remain stored in the moving boundary. Then, the high solute concentration in the moving grain boundary decreases its mobility [22,23] and the boundary ends up stopping at close-to-coherent precipitates. Finally, these close-to-coherent precipitates are fed by the γ'-forming elements stored in the boundary and their coarsening leads to a high pinning force, which definitely prevents the boundary from moving anymore.

The above observations suggest that the recrystallized grains having a <111> axis close to a <111> axis of a recovered grain have an advantage over a randomly-oriented recrystallized grain in consuming it. Yet, consuming a recovered grain amounts to overcoming the high Smith-Zener drag pressure exerted by its close-to-coherent precipitates. For spherical particles, the Smith-Zener drag pressure is usually described by the formula $P_{SZ} = \Gamma.\frac{3f}{2r}$, where Γ, f and r are respectively the grain boundary energy, the precipitate volume fraction and the precipitate mean radius [4]. In the present case, the drag pressure has not been precisely evaluated but, judging from the precipitate density and size, it is very likely to be quite high. In addition, the intragranular precipitates of the recovered grains are close-to-coherent and the drag pressure enforced by coherent precipitates is twice that enforced by the equivalent incoherent population [8,9]. In literature several possible mechanisms to overcome coherent precipitates have been pointed out: precipitates can be bypassed, dissolved (with a coherent re-precipitation behind the recrystallization front) [10,11] or crossed by the recrystallization front so that their orientation is changed to that of the growing grain [7,8]. However here, none of these mechanisms is observed: while many recrystallized grains stop growing very early inside the recovered grain, some recrystallized grains sharing a <111> axis with the recovered grain can grow to a large extent producing T/C type precipitates. Thus, the mechanism leading to T/C type precipitates appears as the more thermodynamically/kinetically interesting mechanism to overcome the precipitates of the recovered grain. Yet, considering that T/C type precipitates are

bounded by {111} planes, this is consistent with a mechanism which minimize the energy of the system since {111} planes are known to be low energy interfaces [24].

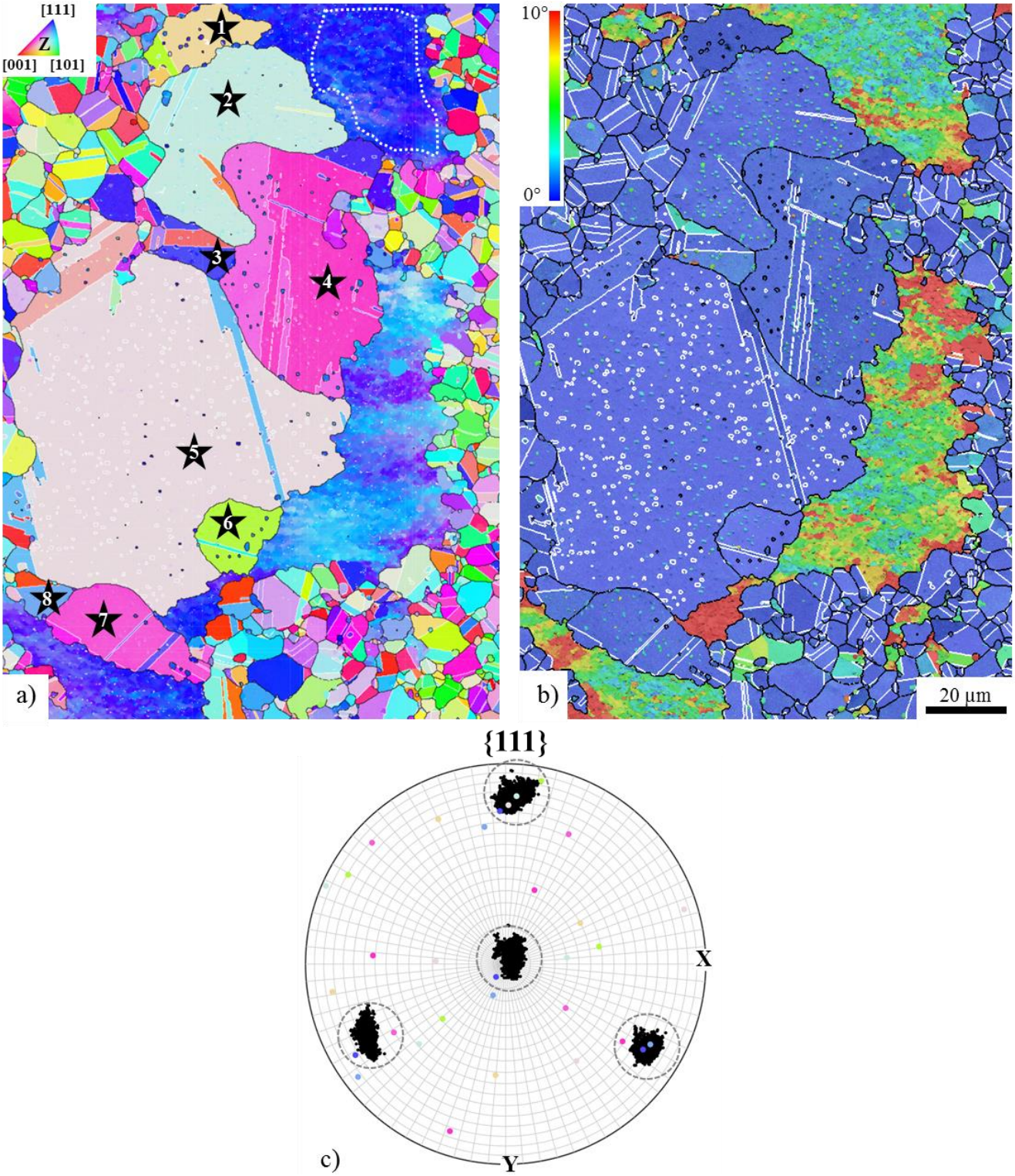

Fig.8 – Analysis of the heterogeneous recrystallization nearby a recovered grain (AD730™ Lab-Forged sample). a) EBSD map: orientation map (IPF color code), grain boundaries (misorientation angle threshold: 10°) plotted black and twin boundaries (60°<111> with 8.66° tolerance) plotted white. b) EBSD map: misorientation angle to the mean grain orientation overlaid on the band contrast map, grain boundaries plotted black and twin boundaries plotted white. c) {111} pole figure on a spherical grid (spacing: 5°), orientations of the recovered grain (white selection in a)) plotted black, orientations of the grains selected by black stars in a) plotted with the same color they appear in a).

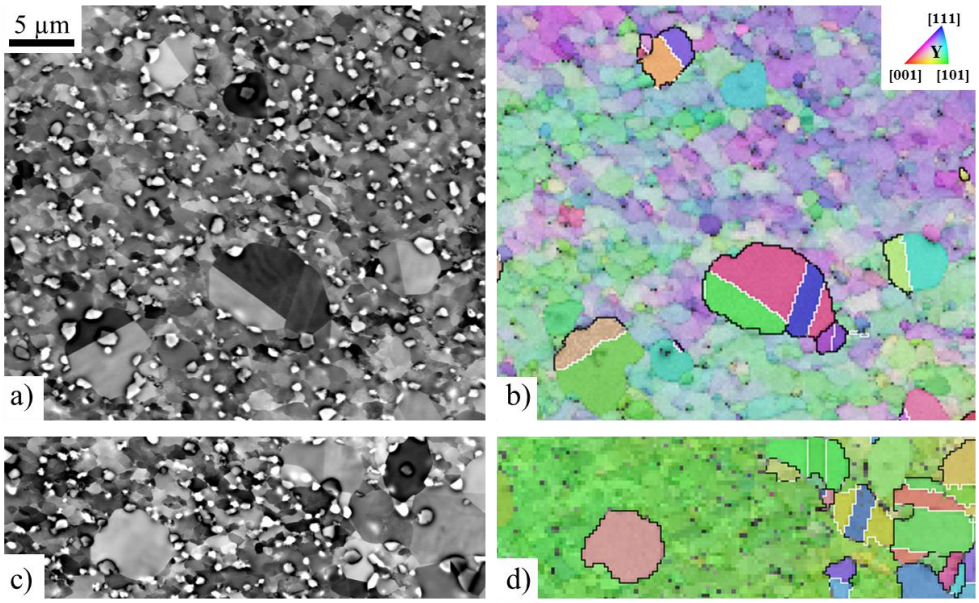

Fig.9 – Recrystallized grains unsuccessful in consuming the surrounding recovered grain (AD730™ Lab-Forged sample). a) and c) Backscattered electron images, where the γ' precipitates appear bright despite their lower atomic number because of topographic effects induced by electropolishing. b) and d) EBSD map: orientation (IPF color code) overlaid on the band contrast maps, grain boundaries (misorientation angle threshold: 10°) plotted black and twin boundaries (60°<111> with 8.66° tolerance) plotted white.

2. Involving grain boundary faceting

As highlighted in [18], the few T-type precipitates evidenced at the recrystallization front (black arrows in Fig.5, Fig.10 and Fig.11) prove that T-type precipitates form at the recrystallization front with their characteristic orientation and facetted shape. Similarly, a C-type precipitate is seen at the recrystallization front in Fig.12.k (black cross).

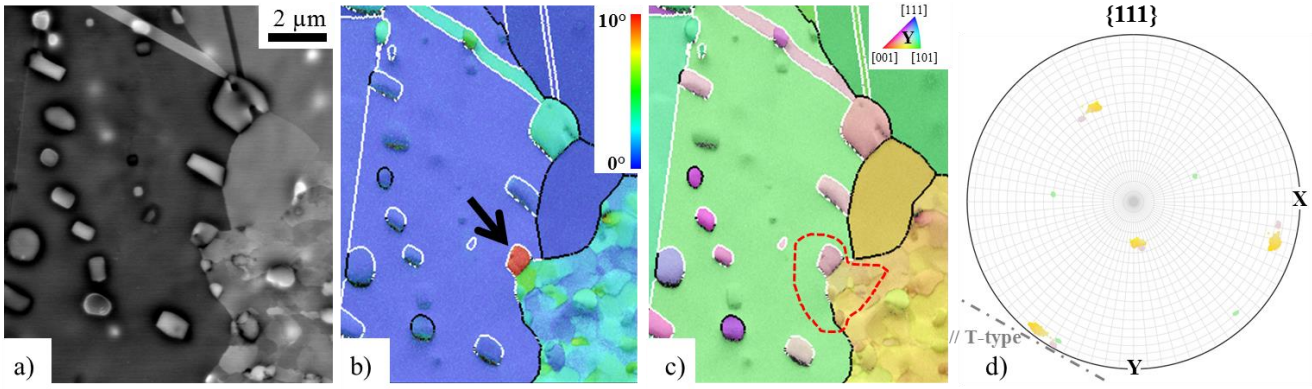

Fig.10 – A T-type precipitate at the recrystallization front in the AD730™ alloy (AD730™ Lab-Forged sample). a) Backscattered electron image, where the γ' precipitates appear bright despite their lower atomic number because of topographic effects induced by electropolishing. b) EBSD map: misorientation angle to the mean orientation of the grain overlaid on the band contrast map, grain boundaries (misorientation angle threshold: 10°) plotted black and twin boundaries (60°<111> with 8.66° tolerance) plotted white. The black arrow underlines a T-type precipitate at the recrystallization front. c) EBSD map: orientation (IPF color code) overlaid on the band contrast map, grain boundaries plotted black and twin boundaries plotted white. d) {111} pole figure on a spherical grid (spacing: 5°), orientations of the red selection in c) plotted with the same color as displayed in c). The {111} plane trace common to the T-type precipitate and the selected matrix is displayed by a dashed line.

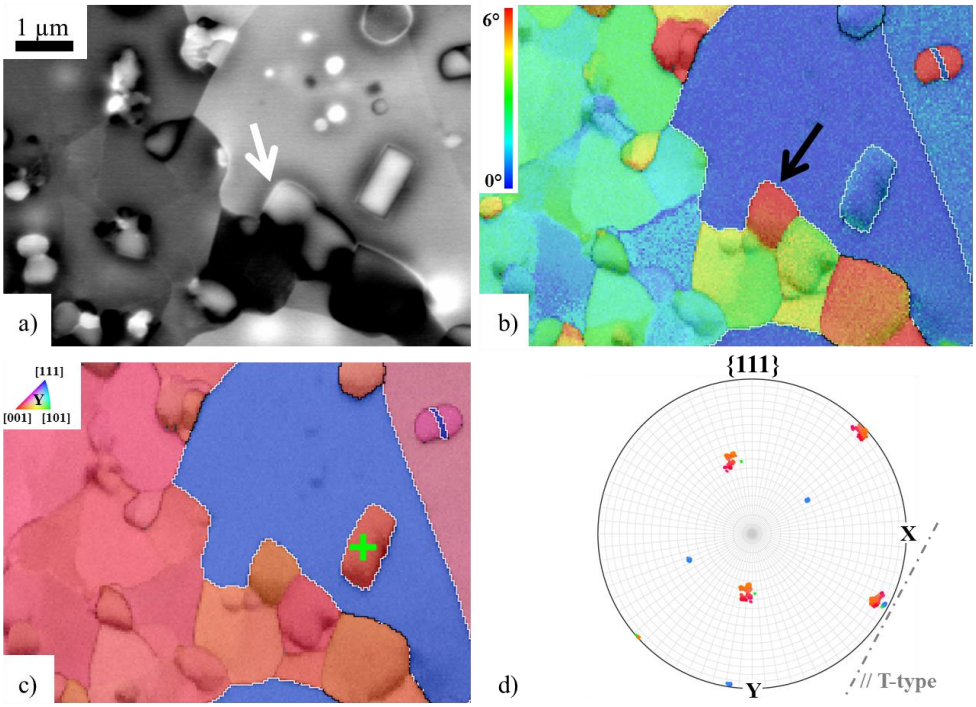

Fig.11 – A T-type precipitate at the recrystallization front in the René65 alloy (René65 billet sample). a) Backscattered electron image, where the γ' precipitates appear bright despite their lower atomic number because of topographic effects induced by electropolishing. The white arrow highlights a grain boundary facet. b) EBSD map: misorientation angle to the mean orientation of the grain overlaid on the band contrast map, grain boundaries (misorientation angle threshold: 10°) plotted black and twin boundaries (60°<111> with 8.66° tolerance) plotted white. The black arrow underlines a T-type precipitate at the recrystallization front. c) EBSD map: orientation overlaid on the band contrast map, grain boundaries plotted black and twin boundaries plotted white. d) {111} pole figure on a spherical grid (spacing: 5°), orientations of the red selection in c) plotted with the same color as displayed in c), orientation of the selected T-type precipitate (green cross in c)) plotted green. The {111} plane trace common to the recrystallized and recovered grains is displayed by a dashed line.

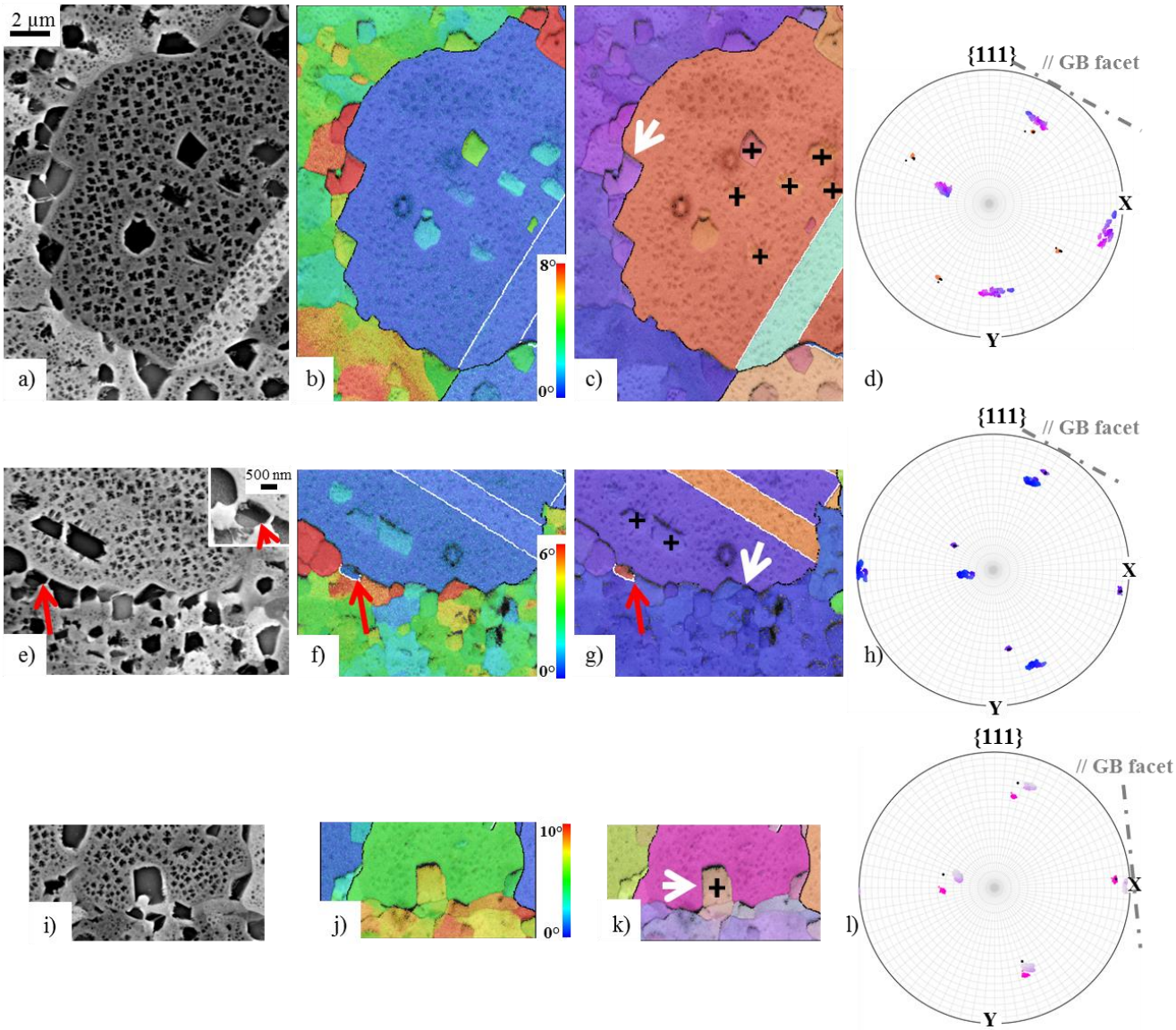

Fig.12 – {111} grain boundary facets at the recrystallization front (AD730™ billet sample). 1st column (a, e and i): Backscattered electron images. Secondary electron image inserted in e), the red arrows point out a twin boundary inside a precipitate. 2nd column (b, f and j): EBSD maps - misorientation angle to the mean orientation of the grain overlaid on the band contrast maps, grain boundaries (misorientation angle threshold: 10°) plotted black and twin boundaries (60°<111> with 8.66° tolerance) plotted white. 3rd column (c, g and k): EBSD maps - orientation (IPF color code) overlaid on the band contrast maps, grain boundaries plotted black and twin boundaries plotted white. The white arrows highlight grain boundary facets. 4th column (d, h and l): {111} pole figures on a spherical grid (spacing: 5°), orientations of the recrystallized/recovered interface plotted with the same color as displayed in the orientation maps, orientations of the selected C-type precipitates (black crosses) plotted black. Some {111} plane traces, parallel to grain boundary facets, are displayed by dashed lines.

In the AD730™ billet sample, small facets in the range of 0.5 to 2 µm wide can be observed on the recrystallized/recovered front (Fig.12). Most of the facets coincide with a {111} plane trace the recrystallized and recovered grains have in common (white arrows on the orientation maps Fig.12). On these facets, precipitates large, facetted and slightly misoriented compared to the neighboring recovered matrix are implanted (misorientation angle to the mean grain orientation maps Fig.12). The insert in Fig.12.e even shows, inside a precipitate implanted on a recrystallization front facet, a twin boundary being itself parallel to the recrystallization front facet. Similarly, in the René65 alloy, the T-type precipitate visible at the recrystallization

front is implanted on a facet which lies on a {111} plane the recrystallized and recovered grains have in common (white arrow in Fig.11.a).

The {111} facets of the T/C type precipitates are very unusual for γ' precipitates since coherent {100} cuboidal γ' precipitates are classically observed in nickel-based superalloys [20,25,26]. Yet, γ' precipitates always evolve so as to minimize the system free energy. For instance, the classical {100} cuboidal shape allows the minimization of the elastic strain energy occurring at the coherent interfaces due to the γ-γ' lattice mismatch. For C/T precipitates, the elastic strain energy is small since their imperfect cube-cube/twin orientation relationships require interfacial dislocations to accommodate the elastic strain. Thus, the morphology and orientations of the C/T type precipitates are mainly controlled by their interfacial energy which has to be minimized considering the recrystallized and recovered sides since C/T type precipitates form at the recrystallization front.

The recrystallized and recovered grains share a <111> axis. Yet, <111>twist boundaries have a much lower boundary energies than any other grain boundary type, with minima at 0°<111> and 60°<111> corresponding to the cube-cube and twin orientation relationships respectively (from [24] the energy of a <111>twist boundary does not exceed 0.5 J/m² while a random boundary can reach 1.5 J/m²). Thus, by developing <111>twist boundaries (approximately) lying on the {111} plane common to the recovered and recrystallized grains, the precipitates decrease their interfacial energy on both recovered and recrystallized sides. Finally, the γ/γ' <111>twist rotation angle which is adopted is the best compromise to minimize the total interfacial energy of the precipitate. This rotation angle is logically close to 0° or 60°, depending on the mutual misorientation of the recrystallized and recovered grains.

Regarding the formation of the {111} facets which have been noticed at the recrystallization front, two hypotheses can be considered; they are schematically represented in Fig.13. The first one (H1) is that the recrystallization front naturally tends to develop {111} facets, and thus <111>twist portions, because of the <111> axis its shares with the recovered grain. Then, due to the supersaturation of the recrystallization front, γ'-forming elements re-precipitate on these {111} facets in order to minimize the total interfacial energy of the obtained precipitates as just explained above. Coincidence Site Lattice (CSL) boundaries naturally tend to facet and the obtained facets are preferentially the crystallographic planes densely packed with coincidence sites [27,28]. Many CSL boundaries in the FCC structure are equivalent to a <111> rotation and so present the {111} planes as densely packed CSL planes. The names of these CSL boundaries as well as their corresponding rotation angle are given in Table 3. One can notice that the <111> rotation angles of these CSL boundaries cover the whole recrystallized/recovered misorientation angle range presented in the present paper (Table 2).

In the second hypothesis (H2), the T/C type precipitates first nucleate at an initially rough recrystallization front due to solute supersaturation. This nucleus is <111> rotated with respect to the recrystallized and recovered grains so as to minimize its interfacial energy. Then, while growing, the precipitate develops its characteristic {111} facets to again minimize its interfacial energy. The γ/γ' {111} facets of the precipitate oblige the recrystallization front in turn to facet so as to bypass it.

At the moment, given the available information, deciding which hypothesis between H1 and H2 is the most likely is not possible. But, whatever the hypothesis considered, as the T/C type precipitates form at the recrystallization front but inside the recovered grain, the recrystallization front still has to bypass them to carry on growing. Because T and C type precipitates are {111} bounded plate-like particles, the classical Smith-Zener

model which is used for spherical particles and, above all, which ignores the interfacial energies between the grains and the particle is not the most appropriate here. However, the work of Ringer et al. [29] on grain boundary pinning by stable cubic-shaped particles is interesting to consider. Indeed, they highlighted that the pinning enforced by a cubic or spherical particle strongly depends the "degree of particle coherency" defined by the ratio:

$$D_{PC} = \frac{\Gamma_{1p} - \Gamma_{2p}}{\Gamma_{12}}$$

Where the grain 1 is non-recrystallized, the grain 2 is recrystallized, Γ_{ip} is the energy of the grain i/particle interface and Γ_{12} is the grain boundary energy. Ringer et al. evidenced that for a cubic (or spherical) particle the pinning force is minimal for low D_{PC} values. On the contrary, in case of a coherent particle, the D_{PC} is close to 1 and the pinning force is much higher. As said above, <111>twist interfaces have low energy values. Thus, considering the T/C type precipitates delimited by <111> twist boundaries whose corresponding {111} plane is common to the recrystallized and recovered grains, Γ_{1p} and Γ_{2p} are very low compared to Γ_{12}, so the D_{PC} is small and the pinning enforced is minimized.

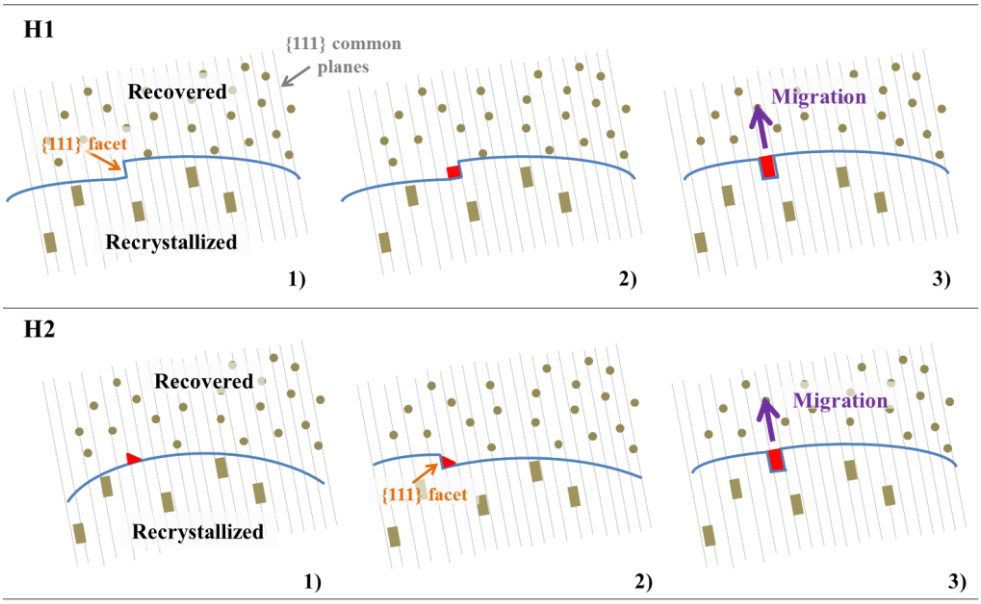

Fig.13 – Schematic diagrams describing the two hypotheses (H1 and H2) for the formation of {111} facets at the recrystallized/recovered front.

3. Scenario proposed for the formation of C and T type precipitates

At this point, a scenario for the formation of T and C type precipitates can be proposed. Under hot-deformation and subsequent heat-treatments, recovered grains partially recrystallize by forming CRX and HERX grains which are low-misoriented to the surrounding recovered matrix. Recrystallized grains are also produced by DRX occurring at the periphery of the recovered grain as everywhere in the equiaxed grain areas. During an annealing stage, all these recrystallized grains start growing inside the recovered grain due to its relatively high stored energy. This first growth step is supported by the dissolution of the precipitates encountered in the recovered grain, so that the recrystallization front gets more and more saturated with γ'-forming elements. Then, there are two cases. In the first case, the recrystallization front gets so saturated that the high solute concentration decreases significantly its mobility. Thus, the recrystallization front stops at some precipitates of the recovered

grain and the γ'-forming elements stored in the front feed those precipitates. Those precipitates coarsen, pin and prevent the boundary from further motion. The second case concerns the recrystallized grains sharing a <111> axis with the nearby recovered grain. These recrystallized grains mainly derive from the CRX and HERX occurring in the recovered grain. The common <111> axis can allow: H1) the formation on the recrystallization front of facets lying on the {111} common planes, then the implantation of γ'-forming elements on the {111} facets as a consequence of supersaturation; H2) the formation of precipitates facetted by the {111} common planes on a rough recrystallization front due to supersaturation, this then obliges the recrystallization front to form {111} facet in order to bypass them. Whatever the hypothesis (H1 or H2), what is sure is that the T/C type precipitates form inside the recovered grain at the recrystallization front, and develop these {111} facets combined with specific orientations to minimize their interfacial energy including both the recrystallized and recovered sides. Indeed, <111>twist boundaries have low energies with minima at 60°<111> and 0°<111>. This implies that the lowest misoriented recrystallized grains (< ~37°) lead to precipitates implanted approximately at 0°<111> on the front, the highest misoriented ones (> ~50°) lead to precipitates implanted approximately at 60°<111> on the front, and that for the intermediate misorientations both implantations are possible. The low interfacial energies on both recrystallized and recovered sides make the facetted precipitates little costly to bypass. The obtained precipitates are few degrees rotated to their host recrystallized grain (~0°<111> - C-type) or in close-to-twin orientation relationship (~60°<111> - T-type). Released from the γ' elements it contained, the recrystallization front can carry on moving inside the recovered grain and repeat the same mechanism. Nevertheless, the scenario which is proposed here has some weaknesses. First, the reason why all the grains derived from the CRX and HERX in the recovered grain do not succeed in growing to a large extent inside the recovered grain is not understood yet. Thus, the mechanism leading to T/C type precipitates must require additional conditions to a common <111> axis to happen. Second, the reason why the γ' precipitates re-arrange inside the recovered grain and not coherently behind the recrystallization front as it is expected from the literature is unclear too. One can imagine that the γ'-forming elements precipitate around a precipitate pre-existing in the recovered grain with a slight change in orientation to minimize the interfacial energy. However, no such sub-boundary has been observed into the T/C type precipitates yet. Another reason which could account for this is the enhanced γ'-forming element diffusion which occurs in the recovered grain due its highly developed network of dislocations [30]. All these points need to be clarified in future research.

IV. CONCLUSION

A previous work [18] has pointed out a close-to-twin orientation relationship between micrometric γ' precipitates and their host recrystallized grain in the AD730™ γ-γ' nickel-based superalloy. The aim of the present paper is to clarify the mechanism leading to such precipitates called T-type precipitates.

This paper shows that:

1. The mechanism leading to T-type precipitates is also able to form C-type precipitates, which are micrometric γ' precipitates slightly misoriented to their surrounding matrix by a rotation of few degrees around a <111> axis. Both C and T type precipitates are found in recrystallized grains which have grown into a recovered grain and which (approximately) share a <111> axis with this recovered grain.

The recrystallized grains sharing a <111> axis with a recovered grain derive from the CRX and HERX occurring in the recovered grain.

2. The misorientation angle between the recrystallized and recovered grains determines if the precipitates are mainly C-type (< ~37°), mainly T-type (> ~50°) or both (between ~37 and ~50°).
3. Both C and T type precipitates are facetted by {111} planes whose corresponding <111> axes are common to the T/C type precipitates, the surrounding recrystallized matrix and the consumed recovered grain.
4. Like the AD730™ alloy, the René65 and PER72 alloys can exhibit large recovered grains. In the René65 and PER72, T and C type precipitates with their characteristic shape and orientation relationships are found in recrystallized grains sharing a <111> axis with the nearby recovered grain. Those recrystallized grains derive from the CRX and HERX mechanisms which have been also pointed out in the recovered grains of the René65 and PER72 alloys. So, the mechanism leading to T/C type precipitates may possibly occur in all the low-lattice-mismatch γ-γ' nickel-based superalloys.
5. The mechanism leading to T/C type precipitates is an advantageous mechanism to overcome the high density of close-to-coherent precipitates in a recovered grain. Thus, regarding a random recrystallized grain, recrystallized grains derived from the CRX and HERX occurring in the recovered grain are privileged for consuming it.
6. T/C type precipitates appear in the recovered grain at the recrystallization front. They grow onto {111} facets that the recrystallization front developed due to its crystallographic structure (H1), or grow directly with {111} facets on a rough recrystallized front which is then obliged to form {111} facets in order to bypass them (H2). Whatever the hypothesis, T/C type precipitates develop <111>twist boundaries with specific rotation angles (~60°<111> and ~0°<111>) in order to minimize their interfacial energy including both the recovered and recrystallized sides. Then, the low interfacial energy on both the recrystallized and recovered sides of the T/C precipitates makes them little costly to bypass.
7. However, some points of the suggested scenario remain unclear. First, as all the CRX and HERX grains formed from the recovered grain do not display T/C type precipitates, additional conditions must certainly be required for the mechanism to happen. Second, the re-precipitation in the recovered grain and not in the recrystallized grain as it is expected from the literature may be perhaps due to the enhanced diffusion occurring in the recovered grain because of its network of dislocations.

ACKNOWLEDGMENTS

This work has been carried out thanks to the financial support of the ANR-Safran industrial chair OPALE.

REFERENCES

1 D. Furrer and H. Fecht: *JOM*, 1999, vol. 51, pp. 14–7.

2 R.C. Reed: *The Superalloys, Fundamentals and Applications*, Cambridge University Press, 2006.

3 R.W. Kozar, A. Suzuki, W.W. Milligan, J.J. Schirra, M.F. Savage, and T.M. Pollock: *Metall. Mater. Trans. A*, 2009, vol. 40, pp. 1588–603.

4 P.A. Manohar and F. Chandra: *ISIJ Int.*, 1998, vol. 38, pp. 913–24.

5 F.C. Campbell: *Elements of Metallurgy and Engineering Alloys*, ASM Intern., 2008.

6 G.S. Rohrer: *J. Mater. Sci.*, 2011, pp. 5881–95.

7 V. Randle and B. Ralph: *Acta Metall.*, 1986, vol. 34, pp. 891–8.

8 R.D. Doherty: *Met. Sci.*, 1982, vol. 16, pp. 1–13.

9 E. Nes, N. Ryum, and O. Hunderi: *Acta Metall.*, 1985, vol. 33, pp. 11–22.

10 R.W. Cahn and P. Haasen: *Physical Metallurgy, Volume I*, North Holland, 1996.

11 A. Porter and B. Ralph: *J. Mater. Sci.*, 1981, vol. 16, pp. 707–13.

12 M.A. Charpagne, P. Vennéguès, T. Billot, J.M. Franchet, and N. Bozzolo: *J. Microsc.*, 2016, vol. 263, pp. 106–12.

13 M. Charpagne, T. Billot, J. Franchet, and N. Bozzolo: *Superalloys 2016*, 2016, pp. 417–26.

14 M.A. Charpagne, T. Billot, J.M. Franchet, and N. Bozzolo: *J. Alloys Compd.*, 2016, vol. 688, pp. 685–94.

15 B.J. Bond, C.M.O. Brien, J.L. Russell, J.A. Heaney, and M.L. Lasonde: *8th Int. Symp. Superalloy 718 Deriv.*, 2014, pp. 107–18.

16 R.S. Minisandram, L.A. Jackman, J.L. Russell, M.L. Lasonde, J.A. Heaney, and A.M. Powell: *8th Int. Symp. Superalloy 718 Deriv.*, 2014, pp. 95–105.

17 C. Crozet, A. Devaux, R. Forestier, S. Charmond, M. Hueller, D. Helm, and W. Buchmann: *Superalloys 2016 Proc. 13th Int. Symp. Superalloys*, 2016, pp. 437–46.

18 S. Vernier, J.-M. Franchet, C. Dumont, P. Vennéguès, and N. Bozzolo: *Scr. Mater.*, 2018, vol. 153, pp. 10–3.

19 D.G. Brandon: *Acta Metall.*, 1966, vol. 14, pp. 1479–84.

20 R.A. Ricks, A.J. Porter, and R.C. Ecob: *Acta Metall.*, 1983, vol. 31, pp. 43–53.

21 G. Nolze and R. Hielscher: *J. Appl. Crystallogr.*, 2016, vol. 49, pp. 1786–802.

22 J. Humphreys, G.S. Rohrer, and A. Rollett: *Recrystallization and Related Annealing Phenomena*, 3rd edn., Elsevier Ltd, 2017.

23 Y. Huang and F.J. Humphreys: *Mater. Chem. Phys.*, 2012, vol. 132, pp. 166–74.

24 D.L. Olmsted, S.M. Foiles, and E.A. Holm: *Acta Mater.*, 2009, vol. 57, pp. 3694–703.

25 A.G. Khachaturyan, S. V. Semenovskaya, and J.W. Morris: *Acta Metall.*, 1988, vol. 36, pp. 1563–72.

26 S.J. Yeom, D.Y. Yoon, and M.F. Henry: *Metall. Mater. Trans. A*, 1993, vol. 24A, pp. 1975–81.

27 B.B. Straumal, O.A. Kogtenkova, A.S. Gornakova, V.G. Sursaeva, and B. Baretzky: *J. Mater. Sci.*, 2015, vol. 51, pp. 382–404.

28 B.B. Straumal, S.A. Polyakov, E. Bischoff, W. Gust, and E.J. Mittemeijer: *Interface Sci.*, 2001, vol. 9, pp. 287–92.

29 S.P. Ringer, W.B. Li, and K.E. Easterling: *Acta Metall.*, 1989, vol. 37, pp. 831–41.

30 R.W. Balluffi: *Phys. Status Solidi*, 1970, vol. 11, pp. 11–34.

31 A. Devaux, B. Picqué, M.F. Gervais, E. Georges, T. Poulain, and P. Héritier: *Superalloys 2012*, 2012, pp. 911–9.

32 H. Grimmer, W. Bollmann, and D.H. Warrington: *Acta Crystallogr. Sect. A*, 1974, vol. 30, pp. 197–207.

TABLES

Table 1 – Chemical compositions of the alloys used in the present work (wt. %)

Element	**Ni**	**Fe**	**Co**	**Cr**	**Mo**	**W**	**Al**	**Ti**	**Nb**	**B**	**C**	**Zr**
AD730™ [31]	Bal.	4.00	8.50	15.70	3.10	2.70	2.25	3.40	1.10	0.01	0.015	0.03
René65 [15]	Bal.	1	13	16	4	4	2.1	3.7	0.7	0.016	-	0.05
PER72	Bal.	0.138	14.5	16.06	2.88	1.21	2.57	5.07	-	0.016	0.017	-

Table 2 – Average misorientation angle $\bar{\theta}$ calculated at recrystallized/recovered grain boundaries

$\bar{\theta}$ at grain boundary	Precipitate Type	REX Grain reference
23.2°	C	Purple crystal in Fig.4.c
24.2°	C	Grain N°2 in Fig.8.a
25.2°	C + 1 single T	Red grain in Fig.2.c
29.7°	C	Grain N°4 in Fig.8.a
31.8°	C	Grain N°6 in Fig.8.a
32.4°	C	Grain N°7 in Fig.8.a
36.3°	C	Orange grain in Fig.12.c
37.7°	C + T	Grain N°5 in Fig.8.a
47.9°	C + T	Purple grain in Fig.5.b
53.2°	T	Orange twin crystals in Fig.4.c
53.8°	T	Green grain in Fig.10.c

Table 3 – CSL boundaries equivalent to a <111> rotation in a FCC structure [32]

CSL boundary	Rotation axis	Rotation angle
Σ3	<111>	60°
Σ7	<111>	38.21°
Σ13b	<111>	27.79°
Σ19b	<111>	46.82°
Σ21a	<111>	21.78°
Σ31a	<111>	17.9°
Σ37c	<111>	50.57°
Σ39a	<111>	32.2°
Σ43a	<111>	15.18°
Σ49a	<111>	43.57°